Title
X-ray tomography study on the crushing strength and irradiation behaviour of dedicated tristructural isotropic nuclear fuel particles at 1000 °C

Authors
Liu, Dong
Knol, Steven
Ell, Jon
et al.

Publication Date
2020-02-01

DOI
10.1016/j.matdes.2019.108382

Peer reviewed

Materials and Design 187 (2020) 108382

Contents lists available at ScienceDirect

Materials and Design

journal homepage: www.elsevier.com/locate/matdes

X-ray tomography study on the crushing strength and irradiation behaviour of dedicated tristructural isotropic nuclear fuel particles at 1000 °C

Dong Liu [a,*], Steven Knol [b], Jon Ell [d], Harold Barnard [f], Mark Davies [e], Jan A. Vreeling [b], Robert O. Ritchie [c,d]

[a] School of Physics, University of Bristol, UK
[b] NRG, Petten, the Netherlands
[c] Department of Materials Science & Engineering, University of California, Berkeley, USA
[d] Materials Sciences Division, Lawrence Berkeley National Laboratory, Berkeley, USA
[e] USNC, Seattle, USA
[f] Advanced Light Source, Lawrence Berkeley National Laboratory, Berkeley, USA

HIGHLIGHTS

- TRISO particles were crushed at 1000 °C with real time X-ray tomography imaging.
- Crack formation and propagation at contact was different from conventional Hertzian contact problem.
- Particles with SiC layer had about 45% reduction in strength at 1000 °C.
- Failure mechanism is different in particles with and without SiC layer.
- Residual stress has potentially impacted the PyC thickness change with neutron irradiation.

GRAPHICAL ABSTRACT

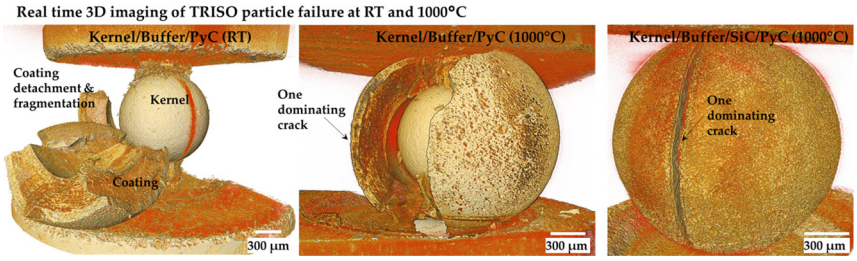

ARTICLE INFO

Article history:
Received 16 August 2019
Received in revised form 20 November 2019
Accepted 21 November 2019
Available online 23 November 2019

Keywords:
TRISO
PYCASSO
High-temperature X-ray computed micro-tomography
Irradiation induced dimensional change
Uniaxial compression
Contact crushing

ABSTRACT

Two types of dedicated Tristructural isotropic (TRISO) nuclear fuel particles, PyC-1 (Kernel/Buffer/PyC) and PyC-2 (Kernel/Buffer/SiC/PyC) from PYCASSO (Pyrocarbon irradiation for creep and swelling/shrinkage of objects) neutron irradiation experiments, were studied. For unirradiated particles, crushing experiments using a unique hot cell, combined with in situ X-ray computed micro-tomography (XCT) imaging, were conducted at room temperature (RT) and at 1000 °C. Although the SiC layer on the particles is presumed to provide 'mechanical stability' to the TRISO particles, results showed a remarkable reduction (~45%) in the crushing strength of the PyC-2 particles at 1000 °C compared to RT. The fracture patterns of the two types of particles, both at the contact zone and on subsequent propagation, differ significantly at RT and 1000 °C. Further, irradiated particles (irradiation temperature: 1000 ± 20 °C; irradiation doses: 1.08–1.23 dpa and 1.49–1.51 dpa) were imaged by XCT; 250 PyC-1 particles and 223 PyC-2 particles were studied in total and the change in radius/layer thickness in each type was examined. It was found that the buffer densification was lower in PyC-1 particles compared to PyC-2 particles, and the PyC layer shrank in the PyC-I particles, whereas it expanded in PyC-2. Results are discussed in terms of how the residual stresses can impact the high-temperature and post-irradiation behavior of these particles.

* Corresponding author.
E-mail address: dong.liu@bristol.ac.uk (D. Liu).

https://doi.org/10.1016/j.matdes.2019.108382

1. Introduction

Since its invention in the United Kingdom as part of the Dragon reactor project [1,2], Tristructural isotropic (TRISO) coated nuclear fuel particles have been used in many different reactors such as Thorium High-Temperature Reactor [3,4] (THTR-300, Germany), HTR-10 [5] (China), the High Temperature Test Reactor [6,7] (HTTR, Japan) and Xe-100 (U.S.) [1]. TRISO is also the fuel form of choice for some designs of the next generation high-temperature gas-cooled reactors (HTGRs) [8] and very-high-temperature reactors (VHTRs) [9] including pebble-bed reactor (PBR) and prismatic-core configurations (e.g., the Russian design of GT-MHR). In addition, TRISO fuel is under consideration for fluoride salt-cooled reactors (FHR) (e.g., by Kairos Power, U.S.) and as a next generation replacement for current uranium pellet fuel in Light Water Reactors (LWRs) [10,11]. It is also adopted by the LWR Fully Encapsulated Fuel (FCM) concept for accident tolerant conditions [12–14].

Specifically, a typical TRISO particle comprises five layers [15], including (i) the fuel kernel (oxide and/or carbide form of Uranium, Plutonium, Thorium or other transuranic elements), (ii) a low density/porous (~50% porosity) pyrolytic carbon layer to act as a buffer to accommodate kernel expansion and a reservoir for fission products, (iii) an inner dense pyrolytic carbon layer (IPyC), (iv) high density/strength SiC layer and (v) an outer PyC layer (OPyC). The SiC layer plays the role of a pressure vessel to withstand the build-up of internal pressure during the fission reaction, and as a barrier for diffusion of gaseous and metallic fission products. It is known that both IPyC and OPyC layers shrink during the early stages of irradiation; as a consequence, the SiC layer is put under compression. Petti et al. [16] compared the fabrication processes between Germany and U.S. TRISO particles and showed that the pyrocarbon anisotropy and density, the IPyC/SiC interface structure, and the SiC microstructure are the three main aspects that could potentially impact the irradiation behaviour of the TRISO particles. Although the buffer layer has been considered the least important in terms of particle integrity, Hunn et al. [17] recently reported that buffer densification counts as one of the main factors that contribute to particle failure in the AGR-1 irradiation experiment.

Since the 1960s, strict process control has led to the fabrication of very high quality particles (~100 defects in 3.3 million particles) in Germany at an industrial/production scale that incorporated improvements from fuel produced for the German AVR and THTR reactors which subsequently supported the HTR-Modul development [16,18]. The U.S. Department of Energy Next Generation Nuclear Plant (NGNP) project [19], where GenIV VHTR was selected to demonstrate emission-free nuclear assisted electricity and hydrogen production, used TRISO as the potential fuel type, specifically, 50 mm diameter pebbles with a graphite matrix for pebble-bed design and 50 mm long by 12.5 mm diameter cylindrical compacts for the prismatic version [19]. This resulted in the Advanced Gas Reactor Fuel Development and Qualification Programme [20,21] (AGR-1 and AGR-2) which focuses on the compact form of these fuel elements with TRISO particles. Similarly, the Korean Nuclear-Hydrogen Technology Development (NHTD) Plan was initiated for irradiation testing of TRISO fuel at the High-flux Advanced Neutron Application Reactor (HANARO) in order to support the development of VHTR in Korea [22–24]. In addition, European based projects, such as the European Commission's Joint Research Centre and the Institute for Energy (JRC-IE), supported a HFR-EU1 irradiation [25] for high burnup of five HTR fuel pebbles to demonstrate its sustainability for conditions beyond that of the current HTR reactor designs with pebble-bed cores.

The particles studied in the present work are from the PYCASSO neutron irradiation experiment [26] (Pyrocarbon irradiation for creep and swelling/shrinkage of objects) at the High Flux Reactor (HFR) in Petten (NRG, The Netherlands). It is part of an integrated project on Very High Temperature Reactors [27], RAPHAEL (Reactor for process heat and electricity). The PYCASSO experiments were to study the impact of high temperature (900–1100 °C) fast neutron irradiation on the thermo-mechanical properties of various coating materials for TRISO-coated particle fuel fabricated by relatively new fabrication processes [28]. The experiment is a separate effect test, where the influence of fuel (coating corrosion or microstructural changes due to fission products), thermal gradients, and variations in coating microstructure and dimensions have been minimized by the use of dummy kernels (Al_2O_3 or ZrO_2), highly conductive particle holder material combined with low energy production of the kernels, and strict (fabrication) quality control and selection procedures, respectively [27]. The detailed rational for the experimental design and the fabrication of the fuel particles can be found in Groot et al. [27]. The particles irradiated in PYCASSO project were provided by CEA (France), JAEA (Japan) and KAERI (Republic of South Korea), which makes this irradiation a truly international GenIV effort.

In particular, CEA particles, with an Al_2O_3 kernel and different buffer, SiC and PyC coating combinations, were used to determine the behaviour of pyrocarbon under irradiation. The ultimate outcome will be used to inform and improve HTR fuel performance modelling. In this work, two out of the four types of CEA particles were characterized. The crushing process of four unirradiated particles was studied at ambient and 1000 °C using in situ X-ray computed tomography (XCT) [29,30] to capture the initiation and propagation of cracks to set out the methodology for future crushing tests on irradiated particles. For the irradiated particles, the radius and thickness changes of each layer were systematically measured using three-dimensional (3D) XCT imaging.

Crushing tests, compared with other more complex geometries such as semi-sphere/shell pressurisation/bending [31–34], were chosen in the present work because it is a promising approach to acquire an estimate of the strength of both unirradiated and irradiated TRISO particles. Owing to its simple test geometry with little sample preparation, it is particularly favoured for post-irradiation studies in hot cells on a large number of samples for performance assessment and quality control [31]. Nevertheless, crushing tests involve a complex contact problem where a localised stress zone is generated by a flattened anvil applied to a sphere particle. The maximum load at failure is affected by the hardness of the anvil [35,36]; high hardness anvils can cause local bending stresses at the contact point with the maximum stress on the inner surface of the SiC, whereas soft loading anvils enable a latitudinal tensile stress on the particle surface. However, the failure process of a crushing test has not been studied by in situ 3D experimental techniques. Briggs et al. [37] used transparent alumina plates for loading and optical stereomicroscopy to examine the tested sample surface; their experiments showed a change in appearance after the first 'pop-in' at ~50% of the maximum load on the load-displacement curve. However, as their observations comprised a 2D projection from the top of a 3D particle, the detailed features of the cracks that formed could not be resolved with accuracy.

In addition, as the coating materials in TRISO particles vary, the failure modes can be quite different, which has not yet been unambiguously characterized [37–39]. More importantly, even though TRISO particles operate at elevated temperatures, all crushing tests reported to date have been performed at room temperature, which can never fully represent the behaviour of these particles at high temperatures. Some authors have studied annealed particles [36,37,40,41] but have needed to cool their samples from above 1000 °C to ambient temperatures to examine them, which could change the cracking configurations and cause radically different residual stress states to form. It is therefore necessary for fidelity to perform in situ crushing experiments on fuel particles at temperature, coupled with a 3D non-destructive imaging technique to correlate in real time the crushing processes to the applied loading and displacement conditions. This was the prime objective of the current study.

2. Materials and experimental procedures

2.1. Materials and neutron irradiation

Four types of CEA particles were irradiated in the PYCASSO project, but only two types of these particles are studied in this work: PyC-1 (Kernel/Buffer/PyC) and PyC-2 (Kernel/Buffer/SiC/PyC), with the former providing the opportunity to study practically unrestrained dimensional changes in the PyC layer and the latter to assess the incorporation of a SiC layer as support. As there is only one PyC layer in PyC-1 and PyC-2, IPyC or OPyC were not differentiated in the following text; it is referred to as PyC for both types of particles. The kernel material was chosen to be corundum (alumina) due to its known behaviour in the reactor and its availability in high-purity form to avoid activation during irradiation. The deposition temperature and gas for buffer carbon, SiC, and PyC were 1350 °C (acetylene with argon), 1560 °C (methyltrichlorosilane with hydrogen) and 1340 °C (acetylene with propylene and argon), respectively [42]. Previous work on these particles [42] showed that the SiC layer comprises columnar cubic β-SiC crystals elongated along the deposition direction with an average size of 1.4 ± 1.2 μm.

These particles were subjected to two different fluences (i.e., ~1.63×10^{25} and ~2.02×10^{25} $n.m^{-2}$ (at an energy of $E > 0.18$ MeV) for PyC-1; details are presented in Table 1) at a well-defined temperature (full temperature range 980°–1020 °C) over 5 HFR cycles (144 full power days). Full details are published elsewhere [26].

2.2. Uniaxial compression at 1000 °C with X-ray tomography on unirradiated particles

In situ high-temperature X-ray tomography experiments were conducted on four unirradiated particles, at beamline 8.3.2 of the Advanced Light Source (Lawrence Berkeley National Laboratory, U.S.). During the experiment, a unique device that permits mechanical loading at elevated temperatures was used [29,30]. Further details of the device can be found in ref. [43]. Briefly, it consists of an in situ ultrahigh-temperature mechanical loading rig mounted inside a ~150 mm diameter water-cooled aluminium sphere that houses six 150 W radiant lamps with elliptical reflectors illuminating a ~5 mm diameter uniform hot zone region in the chamber centre [44]. The particle was positioned on the loading rig to locate at the middle of the thin aluminium window to allow X-ray transmission from the source (monochromatic beam 25 keV) to the detector (PCO Edge 5× CCD camera (2560 × 2560)) through the sample under load. The field of view of 3.3 × 3.5 mm and a pixel size 1.3 × 1.3 μm were achieved. A thermocouple was installed in contact with the particle during heating to control the temperature.

A sample holder with anvils made from alumina (Fig. 1a), mimicking the 'Brazilian disc compression' configuration [45], was designed to apply diametric compression to the particle. To ensure static loading, a displacement rate of 0.5 μm/s was used throughout the experiment. A 3D scan of the whole particle was captured at each loading step until fracture. Real time information of the damage evolution, under load at temperature, in the form of porosity, crack formation and layer thickness changes, were derived from these scans. The tests were conducted at two temperatures: RT and 1000 °C. One particle was tested at each temperature for each type. During each scan, 1969 projections were collected over a standard rotation of 180° that is typical for parallel beam tomography. The acquisition time was 300 ms for each projection. Fifteen flat field images were captured before and after each scan and averaged together. Reconstruction was performed with the Gridrec algorithm in TomoPy package with the centre of rotation of each scan individually identified to account for the deformation in each loading step. During the reconstruction, a conventional (rather than dynamic) flat-field correction method was used to normalise the acquired projection images; this was performed to reduce detector's fixed pattern noise and thereby improve the spatial resolution, and further to correct artefacts such as ring or bands in the reconstructed images.

2.3. 3D imaging using lab-based X-ray tomography on irradiated particles

Lab-based X-ray computed micro-tomography (GE Phoenix Nanotom S tomography system at NRG) was used to characterise the 3D microstructure of approximately 500 particles (250 PyC-1 particles and 223 PyC-2 particles) to investigate the densification kinetics by determining the swelling and shrinkage of the separate layers as a function of fluence. The scans were taken at 80 keV with a 360° rotation; 2300 projections were collected for each scan with a pixel size of 1.9 × 1.9 μm. Knol et al. [46] described in detail the procedures for handling of these irradiated particles; the data were analysed using VSG Avizo 8.1 for image filtering and particle layer segmentation followed by an in-house MATLAB code for quantification, as described by Lowe et al. [47]. Due to the combination of XCT streak artefacts and particle-to-particle contact, the top and bottom 5% of each particle were removed to allow more efficient use of automated segmentation methods and a reduction in the required manual corrections. The details of the experimental setup and image processing have been described by Knol et al. [46]. The radius of the different layers, shown in Fig. 1b, c, were derived with the following steps: (i) determination of the particle centre by calculating the centre-of-mass of the kernel, and then projecting radial lines outward from particle centre over all angles; (ii) polar angles were maintained in the range 0° to 180°, with azimuthal angles in the range 0° to 360°, with the angular step size being 1° for both; (iii) locating the beginning and end of each layer along each radial line.

The dimensions of all the unirradiated particles were measured during the fabrication process at CEA using optical methods; as such, measurements were undertaken between each coating step, with the thickness of each layer being derived to provide a quick and reliable method for determining the outer dimensions of a large number of particles. As the inner layers can be altered by abrasion during the coating process, the dimensions of these layers were determined by destructive measurement techniques on a representative batch afterwards, specifically by grinding to the mid-plane of the particles and determining the layer thicknesses by microscopy; these measurements were subsequently validated by XCT measurements on the unirradiated particles.

3. Results

3.1. Strength degradation with temperature

The uniaxial compression approach used in this work represents a straightforward method to evaluate the nominal strength of both

Table 1
Types of particles and irradiation dose at 1000 °C.

Particle types	Low dose	High dose
PyC-1	1.63 x 10^{25} n·m^{-2} (1.23 dpa in carbon)	2.02 x 10^{25} n·m^{-2} (1.51 dpa in carbon)
PyC-2	1.43 x 10^{25} n·m^{-2} (1.08 dpa in carbon)	1.99 x 10^{25} n·m^{-2} (1.49 dpa in carbon)

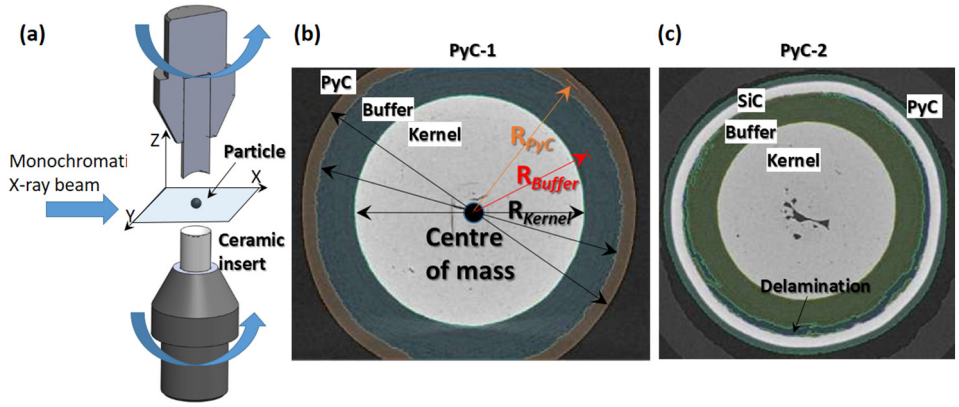

Fig. 1. (a) Schematic illustration of the crushing experiment for the X-ray synchrotron beamline experiments. Segmentation of the NRG XCT scans for the two types of particles: (b) PyC-1 with the definition of the radius of different layers (from the mass centre to the central line of each layer) and (c) PyC-2 showing the buffer/SiC interfacial delamination post irradiation.

unirradiated and irradiated particles, although it is not a standard geometry. As there is a limited number of unirradiated particles available, this experiment was combined with in situ imaging under load using XCT to obtain the exact microstructure and dimensions of the individual layers of each particle to correlate to the load-displacement behaviour; it also provided information to exclude the possibility of an inherent defect-induced strength reduction. Dimensions of each of the layers in the four particles tested are listed in Table 2. Note that there is very little difference (<5%) in the dimensions of the two particles tested for each type. Therefore, it can be concluded that any changes in the loading curves and measured strength levels with temperature are a true reflection of the particle behaviour. Ar gas was used throughout to protect particles from oxidation; although there is no risk of oxidation at RT, for consistency the same gas flow was used at both RT and 1000 °C.

Load-displacement curves for the four tested particles are shown in Fig. 2. It is worth noting that there are other, more sophisticated, geometries and test methods to measure the maximum hoop strain/stress of such spherical particles (e.g., shell crushing [33], semi-sphere internal pressure test [48] and notched particles [49,50]), but processing the irradiated particles into such geometries can be very challenging.

Fig. 2a shows that the two PyC-1 particles failed at a similar maximum load. The PyC-1 particle tested at 1000 °C was dimensionally smaller with all layers slightly thinner than the one tested at RT (Table 1); hence, a lower strength was expected. The PyC-1 particle crushed at 1000 °C showed an extended 'bedding-in' stage. The larger load drops, marked by downward open arrows for RT and upward closed arrows for 1000 °C, are a consequence of ~10 minute holding periods during which XCT scans were collected; however, many smaller load drops were observed, in contrast to the experiments of Briggs et al. [37] where only one drop was reported for each hemisphere. The load drops at 1000 °C are generally more frequent and load relaxation more significant than at RT, e.g., load relaxations of ~6 N are apparent at RT, compared to ~9 N at 1000 °C, for the scans undertaken at 40 N. The small pop-ins in between are most likely due to crushing phenomena and/or the formation of small cracks. Evidence for this from the XCT scans is shown in the following Section 3.2.

The slopes of the load-displacement curves were determined by linear fitting. For RT, a small increase was found at higher loads (i.e., 0.583 ± 0.018 N/μm between 30 and 40 N, rising to 0.655 ± 0.006 N/μm between 45 and 90 N). Similar trends were evident at 1000 °C (i.e., 0.654 ± 0.044 N/μm between 50 and 70 N, and 0.792 ± 0.015 N/μm between 70 and 80 N). It is hard to derive a representative 'modulus' of the particle from these slopes, but this form of behaviour indicates that particle failure is abrupt without significant pre-instability damage, consistent with the XCT observations.

For the PyC-2 particles (Fig. 2b), a ~45% reduction in failure strength occurred at 1000 °C despite the similar dimensions of the two PyC-2 particles (Table 2). While one can suspect that intrinsic defects, such as voids or microcracks, can form in the particle during processing, XCT scans showed no such evidence (see Section 3.2). Rather, it is more likely that the introduction of the SiC layer contributed most to the high temperature strength reduction of the particle. Similar to the PyC-1 particles, the arrows mark the loads at which XCT scans were undertaken. Contrary to the large load drops seen in PyC-1 particles, there was very little load relaxation in the PyC-2 particles at either RT or 1000 °C. The gradients in the load-displacement curves were very consistent; i.e., the PyC-2 particle curve at RT has a gradient of 0.417 ± 0.013 N/μm (at 20 to 30 N) and 0.588 ± 0.018 N/μm (at 35 to 45 N), whereas at 1000 °C, the slopes are 0.395 ± 0.006 N/μm (at 10 to 20 N) and 0.528 ± 0.024 N/μm (20 to 25 N). Both PyC-2 particles failed by brittle fracture at maximum load. Although only one particle was tested at each temperature, the consistency in the load-displacement and fracture behaviour indicates that the reduction in strength is a faithful description of the particle degradation at high temperatures. Further evidence is shown below in the XCT results.

3.2. Fracture processes in particles change with temperature

Four to six tomography scans were collected for each particle tested. In addition to the scans marked by arrows in Fig. 2, XCT scans were also taken for the load-free condition and after final fracture so that the deformation and fracture processes could be followed. Cracks and voids on

Table 2
Dimensions of the four particles tested using in situ XCT.

Type	Test temp (C)	Kernel (μm)	Buffer (μm)	SiC (μm)	PyC (μm)	Whole particle
PyC-1	RT	988.8±7.2	235.5±8.9	N/A	56.6±0.4	1579.4±11.5
PyC-1	1000	982.9±3.6	218.1±11.6	N/A	54.1±3.1	1540.6±14.1
PyC-2	RT	980.1±2.7	184.4±6.7	60.1±2.5	40.8±2.2	1568.1±14.5
PyC-2	1000	976.5±3.2	174.4±6.8	62.8±2.2	39.1±2.1	1543.5±14.6

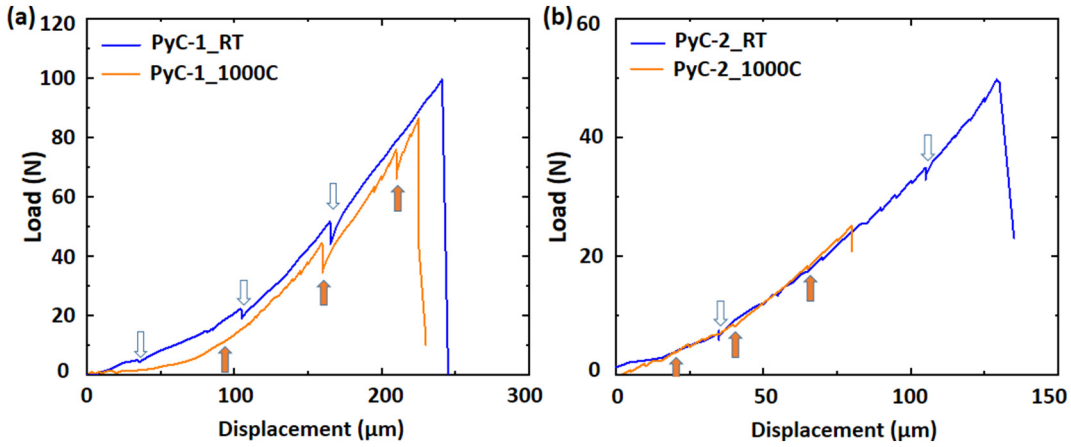

Fig. 2. Load-displacement curves for (a) PyC-1 and (b) PyC-2 particles at RT and 1000 °C. The open arrows pointing downwards and closed arrows pointing upwards are indications of the load at which tomography scans were taken at RT and 1000 °C, respectively.

the order of 2–3 times that of the pixel size were discernible in all scans. The results on primarily two aspects will be presented: (i) the compressive deformation along the loading direction and dilation on the equator plane of the particle, and (ii) the formation of cracks prior to failure and the final fracture patterns.

For the first aspect, two orthogonal slices of the largest diameter, one on the equatorial plane, XY, and the other on the loading plane, XZ, were manually selected, Fig. 3. The diameter was determined in each slice by identifying the edge of the greyscale profile at the particle-air interface. For each slice, 12 measurements, spaced out at 30° intervals, were undertaken, as shown in Fig. 3c. These measurements were then averaged to derive the whole particle diameters in Fig. 3a; the error bar is ±10%, as represented by the size of the symbols.

The PyC-1 particles showed little change in the equatorial plane XY, both at RT and 1000 °C (Fig. 3a), indicating that there is no obvious separation of the different interfaces during deformation until failure. The kernel dimension remained unchanged for all loading steps. When measured along the compressive *z*-axis, though, the height of the particle decreased with increasing load, both at RT and 1000 °C. The gradients describing the change in the whole particle diameter (PyC-

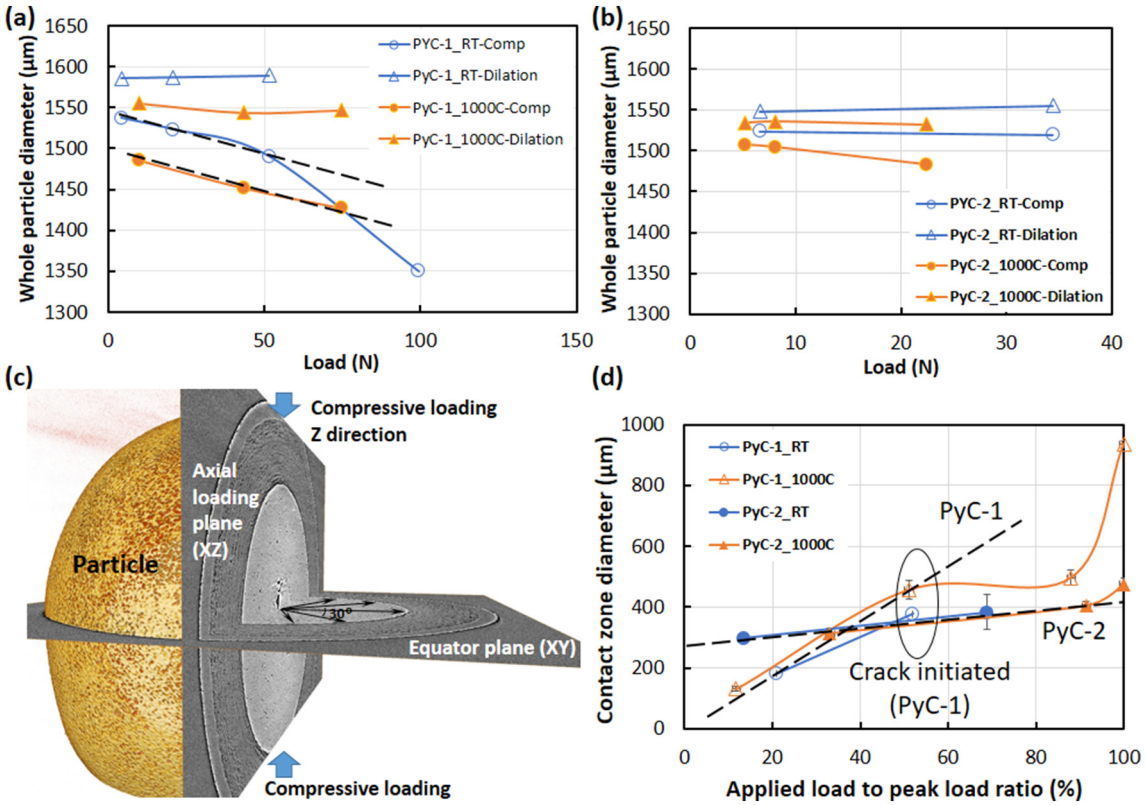

Fig. 3. The change of whole particle dimension along the compressive loading axis (*z*-direction) and equatorial XY plane for (a) PyC-1 particles without a SiC layer and (b) PyC-2 particles with a SiC layer. The error is about ±10% for all measurements; (c) schematic of the equatorial and axial loading planes; (d) the contact area diameter increases with the ratio of applied load to peak load. Each point was an average of seven measurements including four measurements on the circular contact zone when viewed along the loading *z*-axis and three on the XZ plane. Dotted lines are for eye guidance only.

1_1000°C-Comp and PyC-1_RT-Comp) were similar below 75% of the failure load, as indicated by the two parallel dashed lines in Fig. 3a. This was not unexpected as the final failure loads and 'strength' of the two particles were nearly identical (Fig. 2).

PyC-2 particles, due to the presence of SiC layer, deformed much less in the axial *z*-direction both at RT and 1000 °C than the PyC-1 particles (Fig. 3d); additionally, no obvious lateral dilation was observed in the equatorial plane (Fig. 3a). At 1000 °C, the deformation along the compressive *z*-direction was much more pronounced than at RT (*c.f.*, the slope of the curves PyC-2_RT-Comp and PyC-2_1000°C-Comp in Fig. 3b). The change in axial thickness was investigated further by measuring the thickness of each individual layer along the *z*-direction. The results are not plotted in Fig. 3, but it was found that the SiC thickness remained unchanged (within the resolution of the XCT scans) regardless of the load or temperature. However, the PyC and buffer layers together were compressed more along the vertical axis at 1000 °C (~37 μm at 91% failure load) than at RT (~13 μm at 69% failure load, equivalent to 16 μm at 91% failure load using linear extrapolation). Note that without the SiC, the total reduction in thickness by compression in the two layers was similar at both temperatures (e.g., 45 μm at 51.9% failure load for RT and 36 μm at 51.1% failure load). It is apparent that the introduction of SiC layer impacts the depression behaviour of the buffer layer at elevated temperatures, although the cause of this remains unclear.

From Fig. 3a, b, it can be concluded that crushing did not induce obvious expansion of the equatorial plane, as might be seen in fully elastic materials such as a rubber ball. Instead, the deformation was concentrated at the contact points. The mean contact diameters for the PyC-1 and PyC-2 particles are plotted in Fig. 3d as a function of increasing load at each temperature; the load was normalised against the peak failure load. PyC-1 particles had a 20% larger contact area at 1000 °C than at RT, although for loads below 60% of the failure load, the trend was similar at both temperatures. As the load increased, the contact area remained unchanged up to 90% of the failure load, although there was a sudden increase just prior to final fracture. PyC-2 particles, on the other hand, showed a gradual increase in contact area from 300 μm (10 to 30% failure load) to 400 μm (90% failure load) at both RT and 1000 °C. The overall gradient of change was much lower than for PyC-1 particles, consistent with the measurements in Fig. 3a, b where the presence of the SiC layer was found to maintain the shape of the particle.

The initiation of cracking and the overall failure processes in the two types of particles were very different (Fig. 4). For PyC-1 particle at RT, two separated cracks within the contact zone were formed at ~50% failure load (Fig. 4a). These cracks were initially in the PyC layer, then extended vertically down by about 60 μm and stopped in the buffer layer. One of the cracks propagated into a star-shape as it advanced through the PyC-buffer interface (Fig. 4b); consequently, the final failure of this particle was comprised of many fragments (Fig. 4d, f). At 1000 °C, one single splitting crack (40 μm in depth) in the PyC layer was formed at similar load as at RT (Fig. 4c), although this crack subsequently extended to completely split the particle (Fig. 4e, g). The formation of such small cracks is considered to result from the crushing of the PyC layer and are responsible for the pop-ins on the loading curves in Fig. 2.

Due to the lack of real-time 3D imaging techniques in prior studies [37,39,41], the formation of these cracks under load has never been previously captured. As far as the authors are aware, this work shows the first real time 3D imaging of the crushing of TRISO particles at RT and at 1000 °C. Contrary to what has been assumed by most researchers, e.g., by Briggs et al. [37], that the cracks form at a critical distance from the contact zone similar to a Hertzian contact problem, the present work provides no evidence for this as the formation of cracks occurred directly below the loading contact point.

For the PyC-2 particles, it is worth noting that no crack initiation was observed (within the resolution of XCT) prior to final failure. The failure of these particles was abrupt and catastrophic; the fracture patterns at both RT and 1000 °C are shown in Fig. 5. The configuration of the cracks, when viewed downwards along the loading *z*-axis, was closer to a ring shape (Fig. 5a, b). Distinct from the characteristic ring cracks formed outside the contact zone in typical Hertzian contact (due to steep strain gradient on the surface of a flat substrate), the cracks in the PyC-2 particles formed inside the contact zone. Multiple fragmented cracks were formed at RT although much fewer cracks formed inside the ring at 1000 °C. At RT, these cracks penetrated through the PyC and SiC layers before being deflected into the buffer to cause final particle failure (Fig. 5c). Large scale delamination of the SiC-buffer interface was observed. Similar to the PyC-1 particles, fractures at RT were more 'fragmented' with many longitudinal cracks traversing through the three coated layers causing the particle to split into many pieces. In contrast, at 1000 °C, only one straight dominant crack propagated through the SiC and deflected into the buffer layer linking the two polar points of the particle (Fig. 5d, f). The other two small cracks formed at 1000 °C at the contact zone were arrested either in the buffer or SiC-PyC layers before reaching the equatorial plane (Fig. 5b).

One main difference in the crack propagation mechanisms at RT and 1000 °C was that at RT, cracks emanating from the contact zone penetrated through the PyC and SiC layers and then deflected at the SiC-buffer interface for a certain distance before being deflected into the buffer layer. Some of these cracks reached into the kernel to cause kernel-buffer detachment while others terminated in the buffer layer itself (Fig. 5c). At 1000 °C, conversely, crack deflection at the SiC-buffer interface was far less pronounced; instead, the nucleated cracks at the contact zone propagated directly into the buffer layer and then circumvented the particle within this layer (Fig. 5d).

Although for statistical analysis of the quantitative particle strength, a larger number of samples would have to be investigated. The main message here, however, is that real time imaging of the crushing when the particle is still under load is essential to discern the fracture mechanisms. In this regard, it can be concluded that the addition of a SiC layer changed the behaviour with respect to the retention of strength; the cracks initiated within the loading contact zone and the subsequent failure patterns were distinctly different at RT and 1000 °C.

It should be noted that in addition to the crushing behaviour, we also attempted to acquire the coefficient of thermal expansion (CTE) of the whole particle and the individual layers from the XCT scans. For example, for SiC with a CTE of ~5×10^{-6}/K at 1000 °C [15], a change of 0.3 μm was expected which is below the pixel size of the scans. Gilchrist et al. [48] reported PyC to have a higher CTE than SiC of ~6.2×10^{-6}/K up to 500 °C, meaning that the particle, when heated to 1000 °C, would only show a total thickness expansion of ~0.3 μm, i.e., again below our XCT resolution. There was some success with the alumina kernel, where the CTE is reported to be $4.5–8 \times 10^{-6}$/K at 40 to 400 °C [51–54], by manually identifying exactly the same slices (out of 1348 slices of each image stack) of the RT and 1000 °C scans, and then extracting the intensity profile along one of the diametrical directions passing through identical features on these two slices. By comparing the extracted diameter from the exact locations, and repeating this procedure ten times, an average value of $6.2 \pm 0.6 \times 10^{-6}$/K at 1000 °C was acquired, which is consistent with literature values [51–54].

3.3. Changes in radius and thickness after irradiation

Both PyC-1 and PyC-2 fuel particles were irradiated at ~1000 °C to different neutron fluences, as described in Section 2.1 and Table 1. The averaged thickness and radii of all the particles are shown in Table 3, and all the measurements used to derive these average values for the irradiated PyC-1 and PyC-2 particles are plotted in Figs. 6a–c and 7a–d. For simplicity, 1.23 dpa for PyC-1 and 1.08 dpa for PyC-2 are referred to in the graphs as 'low dose' (LD) irradiation and 1.51 dpa for PyC-1 and 1.49 dpa for PyC-2 are referred to as 'high dose' (HD). For both types of particles, the evolution of the average radius and thickness of each layer was presented by normalising with that of the unirradiated

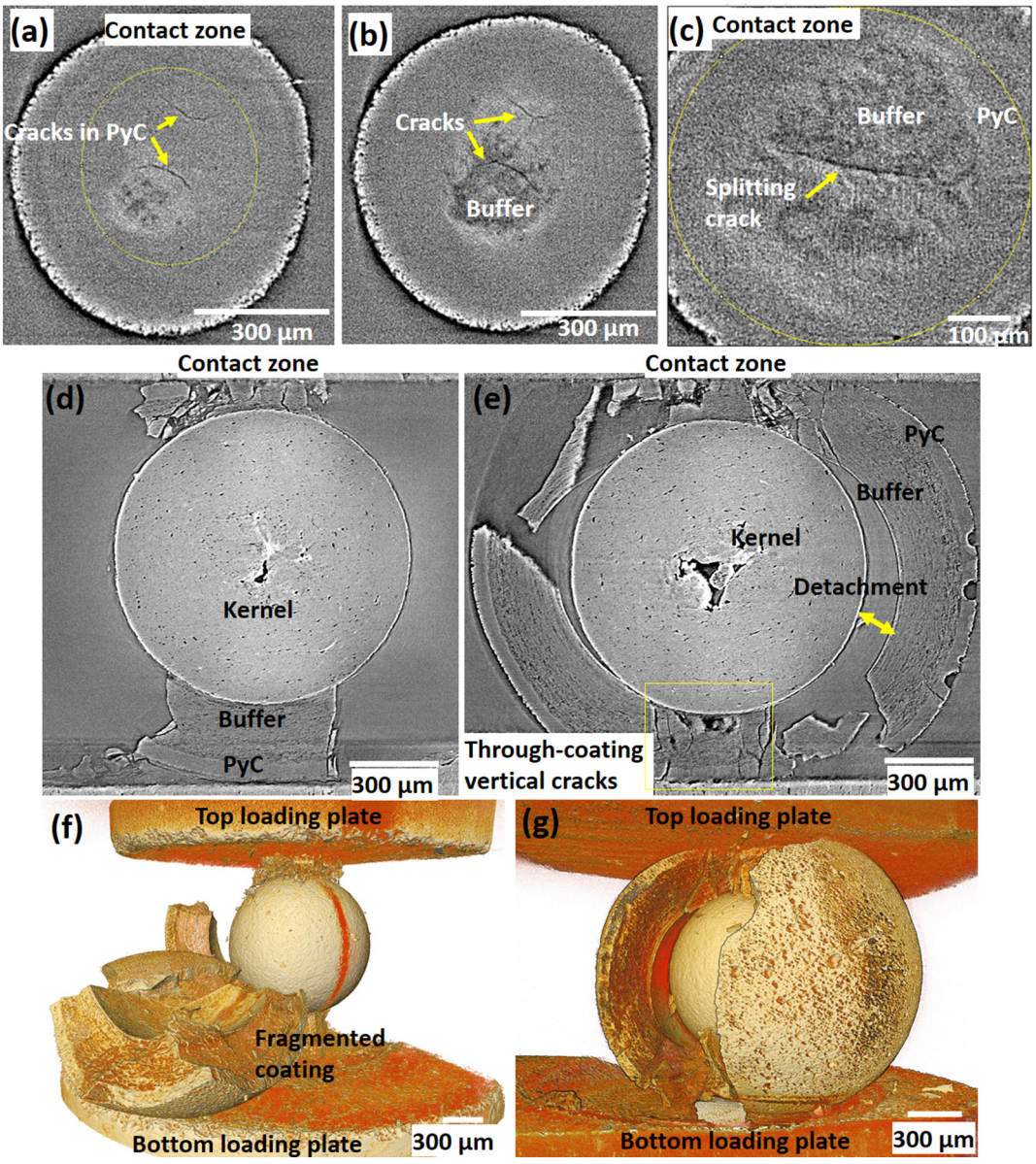

Fig. 4. The initiation of cracks in PyC-1 particles on the XY plane: at (a) RT in the PyC layer, (b) RT at the PyC-buffer interface and (c) at 1000 °C in the buffer layer. Visualisation of the final fracture patterns: (d) 2D (XZ plane) and (f) 3D reconstruction of PyC-1 at RT; (e) and (g) are images of the fracture pattern of the PyC-1 particles at 1000 °C.

particles (Figs. 6d–e and 7e–f). The sizes of the whole particles were calculated by adding the radius of the PyC layer to the PyC layer thickness, as plotted in Figs. 6e and 7f. The standard deviation of the measurements is also included in Table 3; error bars for Figs. 6d–e and 7e–f were estimated to be less than ±4%, i.e., in most part, smaller than the size of the symbols.

Specifically, for the PyC-1 particles, the kernel displayed consistent growth with increased neutron fluence, up to 5.36 µm (i.e., a 0.54% increase in radius) at the high dpa level (Fig. 6d, e). Conversely, the buffer layer showed a clear trend of a decrease in radius as a result of the densification, specifically ~2.0% at low dose and ~2.1% at high dose. The PyC layer correspondingly decreased in radius, ~3.5% at low dose and ~3.7% at high dose, as the buffer-PyC layer interface was well connected (Fig. 6d). A decrease of 31.2 µm, or 13.9% in buffer thickness, was realised at the high fluence, compared to ~12.3% at low dose (Fig. 6e). However, a small increase in the PyC thickness was observed, ~2.1 µm at low dose and ~1.2 µm at high dose. Accordingly, the mean radius of the whole particle was reduced by ~3.6%, mainly from the shrinkage in the buffer layer. No debonding between the layers was observed.

For the PyC-2 particles with a SiC layer located between the buffer and PyC layers, the kernel swelling behaviour was similar to that in the PyC-1 particles (Fig. 7d). For example, at high doses, the relative increase in the kernel radius was ~0.49%, similar to the 0.54% measured in the PyC-1 particles. The buffer radius showed a rapid decrease of ~2.7% with low radiation doses, similar to the 2.6% decrease at high doses, whereas the SiC layer radius remained more or less unchanged (~0.20% shrinkage at low dose and ~0.15% increase at high dose). As expected, the PyC layer, like the SiC layer, displayed a negligible change in radius (~0.29% shrinkage at low dose and a ~0.01% increase at high dose). In terms of thickness changes (Fig. 7f), the same trend of a decrease in the buffer layer thickness was observed in the PyC-2 particles, up to 36 µm (~18.9%) at high dose and ~18.5% at low dose. The increase in SiC thickness was very small (~1.9% at low dose and ~0.6% at high dose). However, the observed reduction in the PyC thickness in the

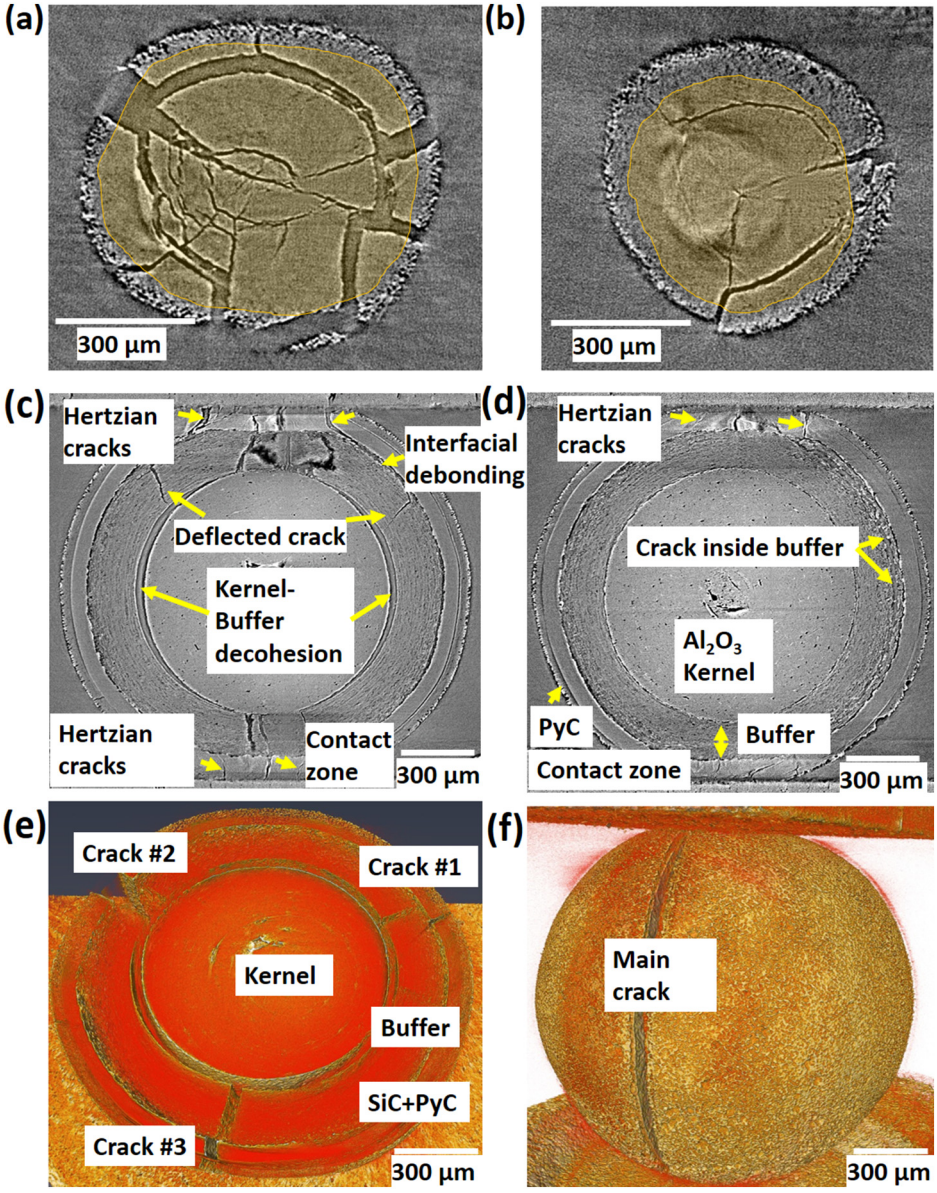

Fig. 5. Contact cracks in PyC-2 particles after final fracture viewed on the XY plane at: (a) RT and (b) 1000 °C, with the contact area marked with shaded circles. Visualisation of the overall final fracture pattern: (c) and (e) are for RT; (d) and (f) were taken at 1000 °C.

PyC-2 particles, i.e., respectively, ~6.8% and ~5.5% at the lower and higher fluence levels, was in contrast to the increase in PyC layer thickness in the PyC-1 particles.

The PyC-2 particles also tended to delaminate between buffer and SiC layers due to densification of the buffer coupled with the shape stability of the SiC. The variation in the delaminated gap size around the particle was quite significant due to the fact that the gap was zero on one side, and at a maximum on the other side. A typical example of this is shown in Fig. 1c. The average gap width of the delamination, i.e., 26.1 ± 2.0 µm for low dose and 28.7 ± 2.4 µm for high dose (Table 3), was consistent with a relatively small standard deviation.

4. Discussion

4.1. Hertzian contact

Usually, a crushing test on TRISO particles is undertaken in compression between two platens, made of either alumina or SiC [37], although aluminium [36] and steel [38,39] have also been used at times, while the load-displacement curves are recorded. Most of these experiments performed to date have been at ambient temperatures and ex situ, i.e., with the process of crack initiation and propagation under load not recorded, which has necessitated assumptions to be made for the interpretation of the results. In the present work, a real time imaging approach was adopted to capture the actual mechanistic aspects of the fracture process under load and at temperature, or following irradiation exposure, in two different types of fuel particles and found significant differences in behaviour (Figs. 4, 5).

In a conventional Hertzian contact problem when two curved surfaces come in contact and deform slightly under the imposed loads, the maximum tensile stress occurs on the surface at a distance away from the contact. The degree of deformation and stress is dependent on the elastic modulus of the two contact materials and varies as a function of the normal contact force and the radii of curvature [55]. In the present compression test set-up utilized to crush the fuel particles, the maximum stress was located inside the contact zone and found to induce vertical cracks. Contrary to the mechanisms suggested by Briggs et al. [37] that the outer coatings would separate at the end of the

Table 3
Number of samples, irradiation temperatures and fluences, and the measured thickness and radius of the coated layers in PyC-1 and Py-2 particles.

Type	DPA (C)	Fluence (10^{25} n/m^2) (E<0.18 MeV)	Irrad. temp (C)	Total number	Kernel (μm)	Whole particle		Buffer (μm)	De-cohesion	SiC (μm)	PyC (μm)
PyC-1	0	0	RT	52	989.8±2.9	1560.9±20.4	Thickness	225.1±9.4	N/A	N/A	59.2±2.1
							Radius	608.4±4.7	N/A	N/A	750.9±9.2
	1.23	1.63	993.2	97	992.9±4.0	1510.2±20.8	Thickness	197.4±8.5	N/A	N/A	61.3±2.1
							Radius	596.2±4.9	N/A	N/A	724.4±9.4
	1.51	2.02	993.9	101	995.2±3.4	1506.2±23.6	Thickness	193.9±10.4	N/A	N/A	60.4±2.4
							Radius	595.4±5.5	N/A	N/A	722.9±10.6
PyC-2	0	0	RT	54	984.7±3.4	1574.2±21.6	Thickness	190.6±10.8	N/A	63.4±1.3	38.4±2.1
							Radius	588.6±5.3	N/A	716.9±9.8	767.9±9.8
	1.08	1.43	1016.0	91	988.1±3.6	1567.2±21.1	Thickness	155.2±9.2	26.1±2.0	64.6±1.3	35.8±2.1
							Radius	572.7±5.1	663.3±9.8	715.4±9.8	765.7±9.5
	1.49	1.99	989.2	78	989.6±3.3	1572.3±21.2	Thickness	154.6±8.7	28.7±2.4	63.7±1.6	36.3±2.1
							Radius	573.0±4.4	664.7±9.1	718.0±9.9	768.0±9.6

Hertzian contact, our direct in situ observations clearly showed that at this stage, the PyC-SiC and buffer layers were all well connected without any discernible separation.

For the PyC-1 particles without the SiC layer, a splitting tensile stress must have formed in the PyC layer at the centre of the contact zone at both RT and 1000 °C, whereas for PyC-2 particles with a hard SiC layer, no prior formation of cracks could be observed before final fracture. The final fracture pattern in the PyC-2 particles was comprised of more complex crack shapes, with angled cracks emanating from the point of contact and the typical circular cracks that usually form outside the contact zone (Fig. 5).

It is worth noting here that alumina was chosen as the contacting plate material to avoid overly concentrated local stresses or crushing. Alumina was the same platen material used by Briggs et al. [37], Cromarty et al. [36] and Rooyen et al. [35]; it has lower hardness and stiffness than SiC (hardness and elastic modulus of alumina is, respectively, 15.7 GPa and 215–413 GPa, compared to 22 GPa and ~460 GPa for SiC [15]), leading to a less localised stress concentration. Admittedly there is a materials mismatch between the platen and the particles, which can cause radial shearing tractions at the interface to resist lateral outwards displacement. Indeed, the contact pressures can become sufficiently high, especially at the centre of the contact zone, to cause a sticking condition which can affect the initiation of surface flaws due to the elevated local stresses and the larger volume of material experiencing such tensile stress. Accordingly, the observed formation of tensile cracks inside the contact zone is not unexpected. A conclusion from our work with real time imaging is to emphasise that one unanimous failure process mechanism cannot be applied to all types of TRSIO particles with different coatings. This must be recognised especially for any evaluation of the strength of such fuel particles as properties will be dependent on the incremental layer coatings that are present [38].

In terms of the quantitative analysis of our results, one should note that Hertz [55] assumed a frictionless normal contact of two elastic bodies with quadratic profiles; the contact of two surfaces with a certain roughness, and hence friction, was not considered until Bowden and

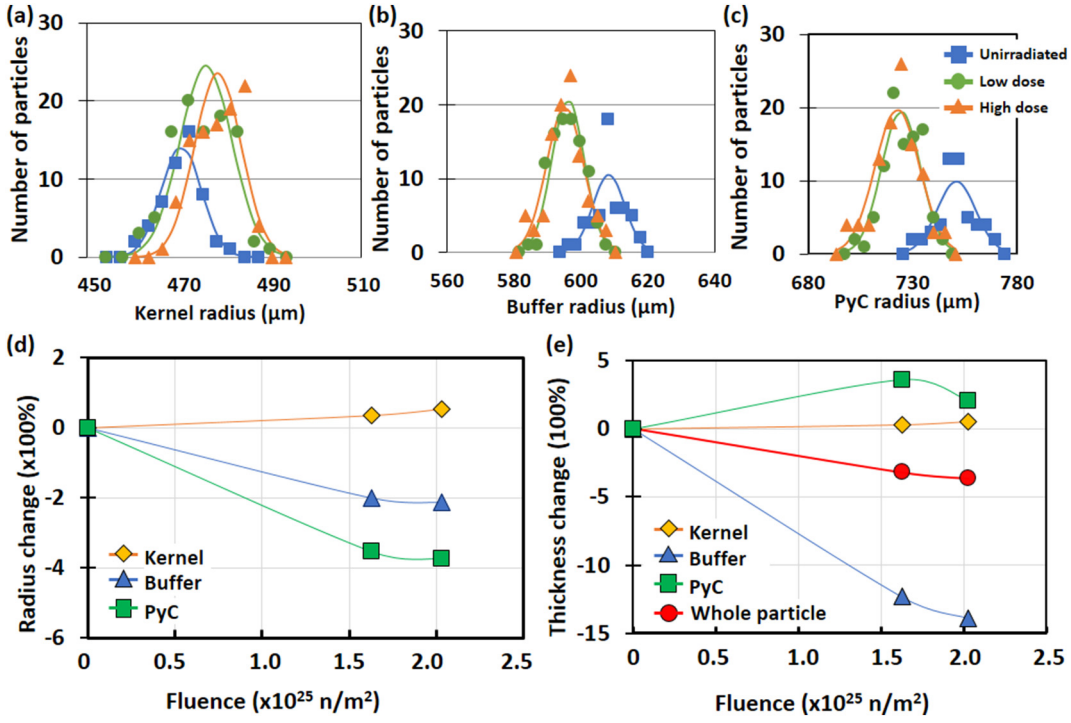

Fig. 6. Measured radii for the (a) kernel, (b) buffer and (c) PyC layers in the PyC-1 particles as a function of fluence at low dose (1.63×10^{25} n/m^2) and high dose (2.02×10^{25} n/m^2) irradiation exposure. Error bars (full width half maximum) are around ±4%. The change in radius and thickness of each layer was normalised using the averaged value extracted from (a)-(c) and presented as percentage changes with irradiation fluence in (d) and (e), respectively.

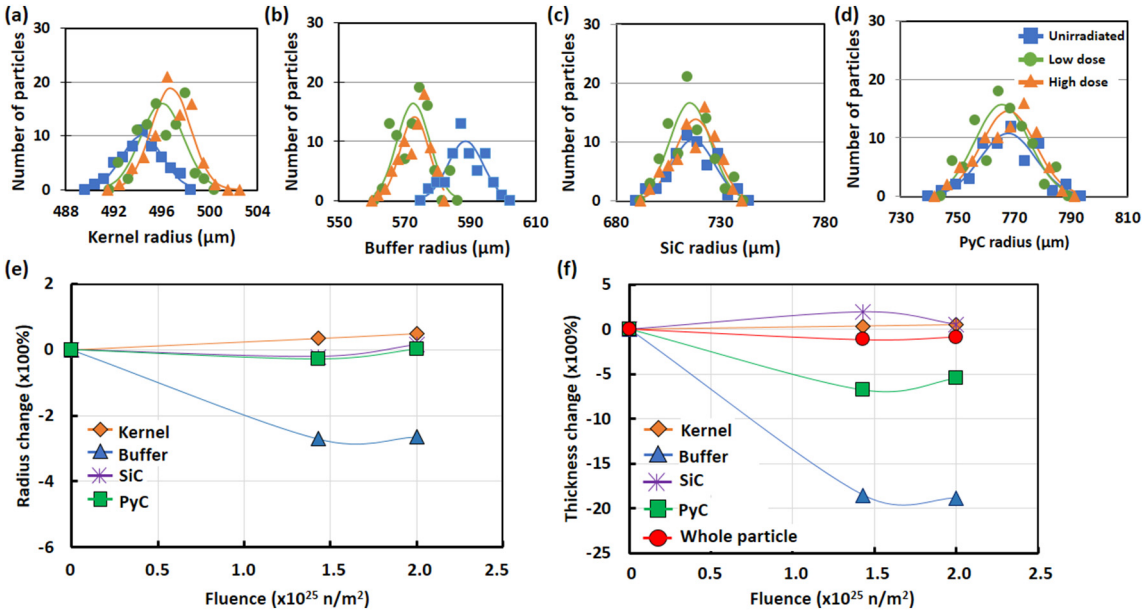

Fig. 7. Measured radii for the (a) kernel, (b) buffer, (c) SiC and (d) PyC layers in the PyC-2 particles as a function of fluence at low dose (1.63×10^{25} n/m^2) and high dose (2.02×10^{25} n/m^2) irradiation exposure. Error bars (full width half maximum) are around ±4%. The change in (e) radius and (f) thickness of each layer was normalised using the averaged value extracted from (a)–(d) and presented as percentage changes with irradiation fluence.

Tabor's work [56,57], which was followed by that of Archard [58], Bush [59] and Persson [60]. In the actual case of crushing a TRISO particle between two platens, both contact surfaces have roughness on many different length-scales, such that the real contact surface will be smaller than the nominal contact area. Assuming both surfaces have asperities with spherical summits with a Gaussian distribution of heights, Archard [58] suggested that the real contact varies linearly with the applied normal load, F_N. Bush et al. [59] approximated the summits by paraboloids and the height distribution by a random distribution and also concluded that, at low loads, the real contact area increases linearly with F_N. Persson et al. [60] later confirmed this result but considered the real contact area to be a factor of $2/\pi$ smaller by considering the lateral coupling between the asperities. In contrast, for ideal frictionless contact, Hertz [55] found the area of contact varies with the applied normal force ~$F^{2/3}$.

The change in measured contact area ($\times 10^4$ μm^2) with applied load for the four particles from Fig. 3 are replotted in Fig. 8 as a function of the applied load, F_N, and 2/3 power of this load, $F_N^{2/3}$. It is worth noting that the XCT results were calculated from the 'nominal contact area' which would approach the 'real contact area' at higher loads. Within measurement error, the nominal contact area appeared to be linearly related to either F_N or $F_N^{2/3}$ over two segments (Fig. 8). The underlying mechanism leading to the two segments is not clear and due to the limited data points, the differences between the two types of particles cannot be resolved. Future work on larger number of unirradiated and irradiated particles would provide more information on this issue.

4.2. Strength reduction in PyC-2 particles at 1000 °C

The PyC-1 particles retained their crushing strength at 1000 °C whereas the PyC-2 particles displayed a marked reduction in strength at elevated temperature. Heat treatment has been found to reduce the crushing load of TRISO particles by as much as 30% [31,38,39,41], but no satisfactory explanation has been proffered. Built-in residual stresses in the SiC, due to the differing thermal expansion coefficient of PyC and SiC, has been considered to be one reason [48].

The possible role of such residual stresses can be examined by considering the relationship proposed for the particle crushing strength by Delle et al. [61] where the strength of the coating material (σ_N) is modelled to be related to the crushing load (F_N), the residual stresses (σ_r) in the coating layer, and the force transmitted to the kernel (F_k) by:

$$\sigma_N = \frac{F_N - F_k}{\pi\left(R_O{}^2 - R_I{}^2\right)} + \sigma_r, \tag{1}$$

where R_I and R_O are the inner and outer radii, respectively, of the coating layer. For the PyC-2 particles, as no obvious change in radius was observed for the outer coating layers (Fig. 3), R_I and R_O can be assumed to be unchanged. The load transmitted to the kernel is hard to estimate but from the XCT measurements, the compression along the loading axis at 1000 °C was clearly higher than at RT (Fig. 3b), which could serve as a direct evidence of an increase in F_k. Although this alone could potentially cause a strength reduction at elevated temperatures according to Eq. (1), another term possibly affecting the strength and failure load is the residual stress, σ_r. As the compressive stress was relaxed at high temperature, the load required to crush particles with the same strength would be smaller than at RT according to Eq. (1). In

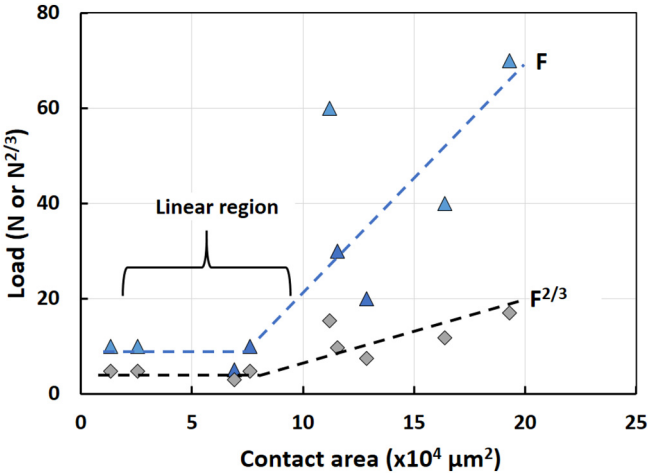

Fig. 8. Relationship between measured contact area and the total load applied (F and $F^{2/3}$).

the present work, a 45% decrease in particle failure load was observed at 1000 °C, which is higher than the 30% reported in the literature [38,39,41]. This is plausible because the literature measurements were undertaken at RT where the residual stresses would have recovered upon cooling down; this would clearly lead to a lower reduction in strength.

Another potential factor for the reduced high-temperature failure load could be due to the degradation of the SiC layer. However, SiC retains its strength quite well at 1000 °C although its elastic modulus can decrease slightly with temperature, as described (with an uncertainty of 5%) by Eq. (2) for temperatures below 1000 K [15]:

$$E = E_0 - 0.04Te^{(-T_0/T)}, \quad (2)$$

where E_0 is the modulus at 0 K but is assumed to be the same as that measured at RT (460 GPa), and T_0 is determined to be 962 K [15], i.e., lower than the ideal Debye temperature of SiC (1123–1126 K [62,63]). Rohbeck et al. [42] measured the elastic modulus and hardness of the SiC layer in the same particles studied in the current work using nano-indentation at RT and 500 °C; results indicated a 40% reduction in nano-hardness at 500 °C and an increase in modulus with irradiation (4% increase in modulus and 7% increase in nano-hardness at a dose of 2.05×10^{25} n·m^{-2}). The decrease in nano-hardness of SiC could potentially indicate a reduction in its yield strength at 1000 °C but this contradicts the known strength retention capability of SiC. Further experiments by Rohbeck et al. [32] on other types of TRISO particles showed that annealing between 1600 °C to 2000 °C had no measurable effect on the nano-scale hardness or modulus of the SiC coating. Therefore, there is no direct evidence to relate the degradation of SiC (strength or elastic modulus) to the reduced strength of the particles.

Thus, the primary cause of the strength reduction in PyC-2 particles at 1000 °C is attributed to the relaxation and re-distribution of residual stresses. In contrast, in the PyC-1 particles, as the maximum failure loads were similar between RT and 1000 °C, we can presume that residual stresses in the PyC and buffer layers are less significant. This is supported by the fact that these two layers have close thermal expansion coefficients, such that fabrication processes would be less likely to induce high built-in stresses. Although a higher compressive depression along the loading axis at 1000 °C was observed in the PyC-1 particles (Fig. 3a), which implies a higher F_k, this did not seem to have influenced the final failure load.

In most studies on fuel particles to date [36–39,41], a large number of particles are generally tested with the strength or failure load presented as a Weibull or normal distribution to evaluate the overall strength. When fractography is undertaken, it is invariably a post mortem examination of the fractured particles where one must assume whether the presence of a large pore, for example, contributed to the low strength of a particular particle. In situ loading of TRISO particles using XCT, especially at elevated temperatures that are representative of service conditions, is thus of critical importance as such higher fidelity tests can reduce the number of experiments required to gain insight into the structural integrity and damage evolution in these particles. Rooyen et al. [35] and Cromarty et al. [36] have remarked that the hardness of the anvils could influence the measured particle strengths and their failure modes, but the present study has clearly demonstrated that changing the coatings of these particles can induce completely different failure modes in a crushing test. Therefore, such real time experiments, even on a small number of particles, are essential for the correct interpretation of results on any TRISO particle crushing test.

4.3. Irradiation induced thickness changes: buffer densification

One of the primary aims of PYCASSO irradiation is to study the irradiation-induced dimensional changes in modern buffer and PyC layers on a spherical TRISO particle configuration. This is one of the factors that made the PYCASSO programme unique in TRISO irradiation studies. Hewette [64] did early work on pyrolytic carbon in ThO_2 microspheres and compared the results with those of Bokros et al. [65] on flat discs; one of the main findings was that the change in initial anisotropy with irradiation on a sphere was more pronounced than on flat discs which subsequently affected the irradiation behaviour of the coatings. Therefore, there is a need to study the coating layers in the eventual geometry of a sphere for a faithful understanding of the irradiation behaviour of TRISO fuel. Other research programmes on coated particles have used real uranium containing kernels; early examples are the NPR-1 and NPR-2 tests at High Flux Isotope Reactor (HFIR, ORNL) and NPR-1A tests at Advanced Test Reactor (ATR, U.S. Idaho National Laboratory), and recent Advanced Gas Reactor Fuel Development and Qualification Programme AGR-1 and AGR-2 (HFIR, ORNL) [17,20,21,66]. With such tests, irradiation can be the confounding variable in light of fission effects such as pressurisation and fission product diffusion. In the present work, only the irradiation effect was studied and by comparing two types of particles, one with restraint (SiC) and the other without, a fundamental understanding of the dimensional changes could be derived to support future modelling of TRISO particle behaviour.

Our study showed that the addition of the SiC layer in PyC-2 particles did not influence the swelling of the kernel. However, the shrinkage of the buffer layer thickness was higher in PyC-2 particles with SiC (~18.9% at high dose) than in PyC-1 particles without SiC (~13.9% at high dose). From the XCT scans, no obvious change in porosity or structure was observed in the buffer layer in PyC-2 particles compared to that in PyC-1 particles (Fig. 9). One possible explanation of the higher buffer shrinkage in the PyC-1 particles could be that their dense outer PyC layer provided constraint to the buffer layer via a strong interface so

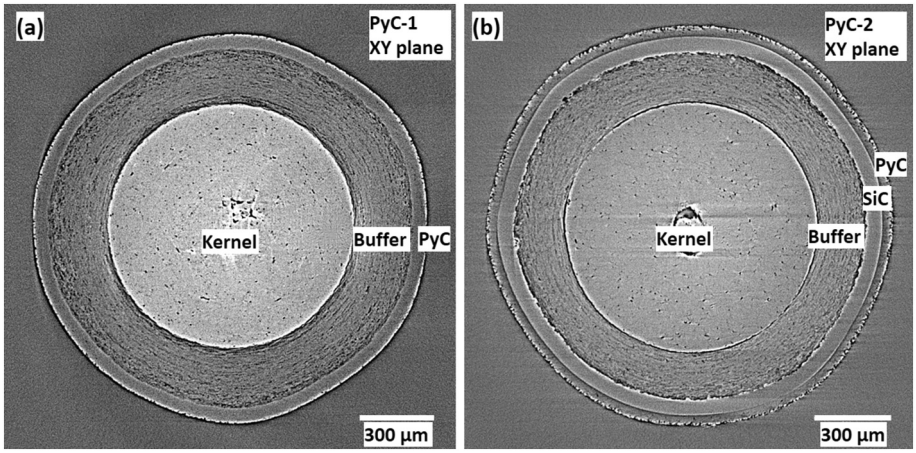

Fig. 9. Middle-plane slices of the (a) PyC-1 and (b) PyC-2 fuel particles, showing the similarity in the microstructure of the buffer layer.

that the latter could not densify freely; this is evident by the fact that no separation between the buffer and PyC layer was found in PyC-1 particles after irradiation. Graphite is known to shrink upon irradiation due to the presence of voids and nano-scale Mrozowski cracks [67]. As the porosity is reduced, the shrinkage becomes less. Thus, it is plausible to assume that the dense PyC material shrinks less than the porous buffer layer and, as such, radial tensile stresses generated in the buffer layer during the irradiation process can inhibit the degree of buffer densification in PyC-1 particles (Figs. 6e and 7f). Moreover, as PyC is not as rigid as SiC, there is benefit in PyC-1 particles with the PyC layer being reduced in radius to some degree due to buffer layer shrinkage, as this acts to alleviate any tendency for separation of the buffer and PyC layer.

In the PyC-2 particles, however, the SiC layer shows negligible dimensional changes and much higher tensile stresses can be generated in the buffer layer during densification; if such tensile stresses exceed the buffer-SiC interface strength, delamination is induced (Fig. 1c). In turn, if such debonding occurs, the buffer layer can contract freely during subsequent irradiation, which results in a large densification and thickness reduction in the PyC-2 particles. Further studies are planned involving residual stress measurements in the buffer layer of unirradiated and irradiated particles in order to provide evidence for the veracity of this hypothesis.

Indeed, there is only very limited literature on buffer layer densification. The most recent report was for UCO-TRISO particles irradiated in an AGR-1 experiment [21] where the buffer volume decreased by 39 ± 2% at peak compact-average burnup of 19.6% fissions per initial metal atom (FIMA) [68]. These measurements were made on polished cross-sections with the volume calculated from the diameter using an ideal sphere assumption. It was found that the UCO kernel also increased in volume by 26 ± 6% and the buffer layer was subjected to internal pressure which enhanced its dimensional change. The thickness variations quantified in the current work (~13.9% in PyC-1 and ~18.9% in PyC-2 particles at high dose) represent significantly smaller volume changes than in the AGR-1 experiment, which is plausible because no internal pressure was applied here; however, it is still hard to compare the two numbers side by side as the equivalent neutron fluence/dpa at 19.6% FIMA was not reported in the AGR-1 experiment [17,20–22].

Another consistent observation between current study and the AGR-1 experiment [22] was the delamination caused by densification of buffer layer; for example, 60% of the AGR-1 particles exhibited complete buffer-IPyC delamination with thin strips of buffer attached to the IPyC layer, and 36% of the particles had radial gaps in the buffer [68]. Ploger et al. [20] studied 981 of such AGR-1 particles and found that 22% showed through-thickness buffer fracture. Despite the assumption that the buffer is the least important layer for fission product retention, Hunn et al. [17] found that, after AGR-1 irradiation or follow-up safety testing, particles with abnormally low cesium retention are typically those with cracked IPyC layers due to shrinkage/fracture of the buffer, as this subsequently exposes the SiC layer to palladium attack. This is considered to be one of the two prime factors in safety tests contributing to the failure of the SiC layers in AGR-1 particles; the other one is related to fabrication defects. Hunn et al. [17] suggested that a low interface strength to promote debonding of the buffer and IPyC layers would be preferable and could further minimize cracking in the IPyC layer. Similar conclusions could be applied to the PyC-2 particles in the current work where a less strong buffer-SiC interface appears to enable an earlier buffer break away during irradiation, thereby generating less stress to the SiC layer. As a separate thermal effect in the crushing experiment on unirradiated particles, a weaker buffer-SiC interface will enable crack deflection and hence a potential increase in resistance to crack growth in the PyC-2 particles. As deftly noted by Nozawa et al. [69], the appropriate interfacial strength is of crucial importance for the functionality of TRISO particles.

The results generated from the current study on buffer densification with separate irradiation effects could provide baseline input to existing modelling. For example, PARFUME models [9,14,70] usually consider only the shrinkage of IPYC and OPYC layers and assume solely elastic deformation in the SiC. Accordingly, with the internal gas pressure of the kernel, the SiC will be under tension such that the fracture of the particles occurs when the tensile stresses exceed the strength of the SiC [71,72]. Effects of buffer shrinkage are not considered, nor its interaction with the IPyC layer; the effects of temperature and buffer densification on the redistribution of stresses across the coated layers are also not accounted for. Detailed discussion of such modelling is outside the scope of the current work, but a thorough, in-depth review of the current state of TRISO fuel performance models is available from Powers and Wirth [70]. It is apparent that key materials properties associated with the buffer and PyC layers as a function of irradiation and temperature are needed, together with some clarification of the role of residual stresses in affecting the fuel performance. It is believed that in situ crushing experiments with real time tomographic observations of the evolution of damage and failure under load and at temperature, as in the current study, can provide essential input to improve the reliability of these models.

4.4. Irradiation-induced thickness changes: PyC thickness changes

A closer inspection of Figs. 6e and 7f indicates a possible change in the trend of thickness in the PyC layer, even though the irradiation fluence in the current work was quite low (e.g., high dose of ~2.02×10^{21} n/cm^2 for PyC-1, Table 3). It is unlikely that the fluences have reached the 'turnaround' point (change from irradiation shrinkage to expansion) that is typical for graphite/carbon materials [67,73]. For example, one of the PyC materials irradiated at 1160° to 1270 °C by Bokros et al. [65] densified first and then swelled at a fluence of 6×10^{21} n/cm^2 (>0.18 MeV). Another PyC sample densified to 2.09 g/cm^3 from 1.8 g/cm^3 when irradiated to 2×10^{21} n/cm^2; this was followed by a decrease in density when the fluence reached 4.5×10^{21} n/cm^2.

One additional marked difference in the irradiation behaviour between the two types of particles is that the PyC layer thickness increased in PyC-1 whereas it decreased in PyC-2. The exact cause for this is not clear, but it could be due to the different residual stress state in the PyC layer in these two particles. As the SiC layer in PyC-2 particles is under compression, the PyC layer is put under tangential tension. As such, the shrinkage in thickness in the PyC layer with irradiation is expected. For the PyC-1 particles, as porous buffer tends to have a larger thermal coefficient of expansion than PyC layer, the PyC layer is most likely to be under compression, which induces an increase in the thickness with irradiation. Future work on residual stress measurement and irradiation induced damage on the polished cross-sections of irradiation particles will provide evidence in this regard.

5. Summary and conclusions

This work was focused on an experimental study of dedicated CEA TRISO nuclear fuel particles in the PYCASSO programme, which were subjected to irradiation and to in situ crushing experiments at ambient to high temperatures with real time X-ray micro-tomography imaging of the resulting damage and dimensional changes.

Four unirradiated particles were crushed with in situ XCT observations at room temperature and at 1000 °C. For PyC-1 particles, comprising a Kernel/Buffer/PyC architecture, microcracks were formed at the loading contact point and propagated to cause failure of the particles at both temperatures. For PyC-2 particles, with a Kernel/Buffer/SiC/PyC architecture, no obvious pre-cracking was observed prior to outright failure which was abrupt. In both cases, the cracks emanating from the loading contact point, either prior to or after final failure, were all located within the contact zone, i.e., quite distinct from the conventional Hertzian contact model. This methodology developed for real time observation of crack initiation and propagation will be applied to future

modelling of irradiated particles subjected to mechanical degradation under crushing loading.

Additionally, 250 PyC-1 particles and 223 PyC-2 particles subjected to neutron irradiation were measured to evaluate changes in their radius and thickness in the different coating layers as a function of fluence. It was found that the buffer layer shrank less in the PyC-1 particles because of its strong interface with the PyC layer; in contrast, in the PyC-2 particles, the buffer layer tended to break away from the SiC layer due to increased shrinkage in the buffer even after low dose irradiation. The PyC layer was found to thicken in the PyC-1 particles and thinned in the PyC-2 particles with irradiation. The exact cause for this is currently unclear but reasoned to be primarily attributed to residual stresses. The outcome of this work will be implemented to the design and processing of TRISO particles.

CRediT authorship contribution statement

Dong Liu: Conceptualization, Data Curation, Formal analysis, Funding acquisition, Investigation, Methodology, Supervision, Writing - original draft. **Steven Knol, Mark Davies, Jan A. Vreeling:** Conceptualization, Funding acquisition, Recources. **Jon Ell, Harold Barnard:** Investigation. **Robert O. Ritchie:** Resources, Funding acquisition, Supervision, Writing - review&editing.

Declaration of competing interest

The authors declare that they have no known competing financial interests or personal relationships that could have appeared to influence the work reported in this paper.

Acknowledgements

The authors would like to thank the ARCHER project and the Ministry of Economic Affairs from the Netherlands for funding this work. D.L. acknowledges funding from the EPSRC fellowship grant no. EP/N004493/1 and the Royal Commission for the Exhibition of 1851 Research Fellowship grant. The authors acknowledge the use of the X-ray synchrotron micro-tomography beamline (8.3.2) at the Lawrence Berkeley National Laboratory's Advanced Light Source, which is supported by the U.S. Department of Energy, Office of Science, Office of Basic Energy Sciences of the U.S. Department of Energy under contract no. DE-AC02-05CH11231. D.L. and R.O.R. would like to thank Dr. Dula Parkinson for his help with these tomography experiments. For the results obtained from the NRG tomography, the data image cutting, filtering and segmentation were performed by Mr. Xuekun Lu, Miss Bo Yu, Mr. Xun Zhang and Miss Ying Wang. This work was supervised and directed by Dr. Tristan Lowe. The data analysis using MATLAB was performed by Dr. Robert Bradley.

Data availability

The raw data and the processed data required to reproduce these findings are available from the corresponding author on reasonable request.

References

[1] Y. Brits, F. Botha, H. van Antwerpen, H.-W. Chi, A control approach investigation of the Xe-100 plant to perform load following within the operational range of 100 – 25 – 100%, Nucl. Eng. Des. 329 (2018) 12–19.
[2] J.M. Beck, L.F. Pincock, High Temperature Gas-Cooled Reactors Lessons Learned Applicable to the Next Generation Nuclear Plant, INL/EXT-10-19329, 2011.
[3] K. Rollig, W. Theymann, Operational Requirement of Spherical HTR Fuel Elements and Their Performance, Specialists' Meeting on Gas-Cooled Reactor Fuel Development and Spent Fuel Treatment, 1985.
[4] H. Nickel, H. Nabielek, G. Pott, A. Mehner, Long time experience with the development of HTR fuel elements in Germany, Nucl. Eng. Des. 217 (2002) 141–151.
[5] M. Lang, H. Xie, Y. Dong, Three design basis accidents' analysis on the HTR-10GT, Sci. Technol. Nucl. Install. 2017 (2017) 1–13.
[6] K. Fukuda, et al., Research and development of HTTR coated particle fuel, J. Nucl. Sci. Technol. 28 (1991) 570–581.
[7] S. Saito, T. Tanaka, Y. Sudo, Design of High Temperature Engineering Test Reactor (HTTR), JAERI 1332, 1994.
[8] T. Taryo, et al., The development of HTGR-TRISO coated fuels in the globe: challenging of Indonesia to be an HTGR fuel producer, J. Phys. Conf. Ser. 1198 (2019), 022062.
[9] B. Liu, T. Liang, C. Tang, A review of TRISO-coated particle nuclear fuel performance models, Rare Metals 25 (2006) 337–342.
[10] K.A. Terrani, L.L. Snead, J.C. Gehin, Microencapsulated fuel technology for commercial light water and advanced reactor application, J. Nucl. Mater. 427 (2012) 209–224.
[11] J. Porta, et al., Coated particle fuel to improve safety, design, economics in water-cooled and gas-cooled reactors, Prog. Nucl. Energy 38 (2001) 407–410.
[12] K.A. Terrani, et al., Fabrication and characterization of fully ceramic microencapsulated fuels, J. Nucl. Mater. 426 (2012) 268–276.
[13] K.A. Terrani, L.L. Snead, J.C. Gehin, FCM fuel development for SMR applications, ASME 2011 Small Modular Reactors Symposium, ASME 2011, pp. 207–209, https://doi.org/10.1115/SMR2011-6608.
[14] J.J. Powers, et al., Fully Ceramic Microencapsulated (FCM) Replacement Fuel for LWRs, Oak Ridge National Laboratory, 2013https://doi.org/10.2172/1087039.
[15] L.L. Snead, et al., Handbook of SiC properties for fuel performance modeling, J. Nucl. Mater. 371 (2007) 329–377.
[16] D.A. Petti, J. Buongiorno, J.T. Maki, R.R. Hobbins, G.K. Miller, Key differences in the fabrication, irradiation and high temperature accident testing of US and German TRISO-coated particle fuel, and their implications on fuel performance, Nucl. Eng. Des. 222 (2003) 281–297.
[17] J.D. Hunn, et al., Detection and analysis of particles with failed SiC in AGR-1 fuel compacts, Nucl. Eng. Des. 306 (2016) 36–46.
[18] D. Petti, et al., The DOE advanced gas reactor fuel development and qualification program, JOM 62 (2010) 62–66.
[19] Southworth, F. H. et al. The Next Generation Nuclear Plant (NGNP) Project.
[20] S.A. Ploger, P.A. Demkowicz, J.D. Hunn, J.S. Kehn, Microscopic analysis of irradiated AGR-1 coated particle fuel compacts, Nucl. Eng. Des. 271 (2014) 221–230.
[21] P.A. Demkowicz, et al., Irradiation performance of AGR-1 high temperature reactor fuel, Nucl. Eng. Des. 306 (2016) 2–13.
[22] B.G. Kim, et al., The first irradiation testing and PIE or TRISO-coated particle fuel in Korea, Nucl. Eng. Des. 329 (2018) 34–45.
[23] B.G. Kim, et al., Irradiation device for irradiation testing of coated particle fuel at HANARO, Nucl. Eng. Technol. 45 (2013) 941–950.
[24] J.M. Park, et al., Analysis on the post-irradiation examination of the HANARO miniplate-1 irradiation test for kijang research reactor, Nucl. Eng. Technol. 49 (2017) 1044–1062.
[25] M. Laurie, A. Marmier, G. Berg, J.-M. Lapetite, C. Tang, Results of the HFR-EU1 fuel irradiation of INET and AVR pebbles in the HFR Petten, Nucl. Eng. Des. 251 (2012) 117–123.
[26] S. Knol, S. de Groot, P.R. Hania, M.H.C. Hannink, PYCASSO: irradiation of HTR coated particles at high temperatures, Nucl. Eng. Des. 251 (2012) 150–156.
[27] S. de Groot, et al., RAPHAEL-FT generation IV PYCASSO-I irradiation, Fourth International Topical Meeting on High Temperature Reactor Technology, Volume 2, ASME 2008, pp. 337–346, https://doi.org/10.1115/HTR2008-58127.
[28] S. de Groot, et al., HTR fuel coating separate effect test PYCASSO, Nucl. Eng. Des. 240 (2010) 2392–2400.
[29] D. Liu, B. Gludovatz, H. Barnard, M. Kuball, R.O. Ritchie, Damage tolerance of nuclear graphite at elevated temperatures, Nat. Commun. 8 (2017).
[30] H.A. Bale, et al., Real-time quantitative imaging of failure events in materials under load at temperatures above 1,600°C, Nat. Mater. 12 (2012) 40–46.
[31] S.-G. Hong, T.-S. Byun, R.A. Lowden, L.L. Snead, Y. Katoh, Evaluation of the fracture strength for silicon carbide layers in the tri-isotropic-coated fuel particle, J. Am. Ceram. Soc. 90 (2007) 184–191.
[32] N. Rohbeck, P. Xiao, Evaluation of the mechanical performance of silicon carbide in TRISO fuel at high temperatures, Nucl. Eng. Des. 306 (2016) 52–58.
[33] P. Hosemann, et al., Mechanical characteristics of SiC coating layer in TRISO fuel particles, J. Nucl. Mater. 442 (2013) 133–142.
[34] T.S. Byun, J.D. Hunn, J.H. Miller, L.L. Snead, J.W. Kim, Evaluation of fracture stress for the SiC layer of TRISO-coated fuel particles using a modified crush test method, Int. J. Appl. Ceram. Technol. 7 (2009) 327–337.
[35] G.T. van Rooyen, R. du Preez, J. de Villiers, R. Cromarty, The fracture strength of TRISO-coated particles determined by compression testing between soft aluminium anvils, J. Nucl. Mater. 403 (2010) 126–134.
[36] R.D. Cromarty, G.T. van Rooyen, J.P.R. de Villiers, Crush strength of silicon carbide coated TRISO particles: influence of test method and process variables, J. Nucl. Mater. 445 (2014) 30–36.
[37] A. Briggs, R.W. Davidge, C. Padgett, S. Quickenden, Crushing behaviour of high temperature reactor coated fuel particles, J. Nucl. Mater. 61 (1976) 233–242.
[38] T. Ogawa, K. Ikawa, Crushing strengths of SiC-Triso and ZrC-Triso coated fuel particles, J. Nucl. Mater. 98 (1981) 18–26.
[39] K. Minato, K. Fukuda, K. Ikawa, H. Matsushima, S. Kurobane, Crushing strength of irradiated Triso coated fuel particles, J. Nucl. Mater. 119 (1983) 326–332.
[40] J. van Rooyen, J.H. Neethling, P.M. van Rooyen, The influence of annealing temperature on the strength of TRISO coated particles, J. Nucl. Mater. 402 (2-3) (2010) 136–146.
[41] W.J. Lackey, D.P. Stinton, L.E. Davis, R.L. Beatty, Crushing strength of high-temperature gas-cooled reactor fuel particles, Nucl. Technol. 31 (1976) 191–201.
[42] N. Rohbeck, et al., In-situ nanoindentation of irradiated silicon carbide in TRISO particle fuel up to 500 °C, J. Nucl. Mater. 465 (2015) 692–694.

[43] A. Haboub, et al., Tensile testing of materials at high temperatures above 1700 °C with in situ synchrotron X-ray micro-tomography, Rev. Sci. Instrum. 85 (2014), 083702.
[44] A.A. Macdowell, et al., High temperature x-ray micro-tomography, 1741 (2016), 50005.
[45] G.E. Andreev, A review of the Brazilian test for rock tensile strength determination. Part I: calculation formula, Min. Sci. Technol. 13 (1991) 445–456.
[46] S. Knol, P.R. Hania, B. Janssen, M. Heijna, S. de Groot, PYCASSO: X-ray tomography on HTR coated particles, Nucl. Eng. Des. 271 (2014) 206–208.
[47] T. Lowe, et al., Microstructural analysis of TRISO particles using multi-scale X-ray computed tomography, J. Nucl. Mater. 461 (2015) 29–36.
[48] K.E. Gilchrist, J.E. Brocklehurst, A technique for measuring the strength of high temperature reactor fuel particle coatings, J. Nucl. Mater. 43 (1972) 347–350.
[49] A.A. Wereszczak, O.M. Jadaan, H.-T. Lin, G.J. Champoux, D.P. Ryan, Hoop tensile strength testing of small diameter ceramic particles, J. Nucl. Mater. 361 (2007) 121–125.
[50] A.A. Wereszczak, T.P. Kirkland, O.M. Jadaan, Strength measurement of ceramic spheres using a diametrally compressed C-sphere specimen, J. Am. Ceram. Soc. 90 (2007) 1843–1849.
[51] Properties: alumina - Aluminium oxide - Al2O3 - a refractory ceramic oxide, Available at https://www.azom.com/properties.aspx?ArticleID=52.
[52] P. Auerkari, Mechanical and physical properties of engineering alumina ceramics, VTT Manufacturing Technology Report, 1996.
[53] A.M. Huntz, L. Maréchal, B. Lesage, R. Molins, Thermal expansion coefficient of alumina films developed by oxidation of a FeCrAl alloy determined by a deflection technique, Appl. Surf. Sci. 252 (2006) 7781–7787.
[54] D. Kuscer, I. Bantan, M. Hrovat, B. Malič, The microstructure, coefficient of thermal expansion and flexural strength of cordierite ceramics prepared from alumina with different particle sizes, J. Eur. Ceram. Soc. 37 (2017) 739–746.
[55] H. Hertz, On the Contact of Rigid Elastic Solids and Hardness, 1882.
[56] Frank P. Bowden, D. Tabor, The area of contact between stationary and moving surfaces, Proc. R. Soc. London. Ser. A. Math. Phys. Sci. 169 (1939) 391–413.
[57] F.P. Bowden, D. Tabor, The Friction and Lubrication of Solids, Clarendon Press, 2001.
[58] J.F. Archard, Elastic deformation and the laws of friction, Proc. R. Soc. London. Ser. A. Math. Phys. Sci. 243 (1957) 190–205.
[59] A.W. Bush, R.D. Gibson, T.R. Thomas, The elastic contact of a rough surface, Wear 35 (1975) 87–111.
[60] B.N.J. Persson, F. Bucher, B. Chiaia, Elastic contact between randomly rough surfaces: comparison of theory with numerical results, Phys. Rev. B 65 (2002), 184106.
[61] W. Delle, K. Drittler, G. Haag, H. S. JUL-569-RW. ORNL-tr-2128, 1969.
[62] C. Kittel, Introduction to Solid State Physics, 1976.
[63] A. Zywietz, K. Karch, F. Bechstedt, Influence of Polytypism on Thermal Properties of Silicon Carbide, 1996.
[64] D.M. Hewette, High temperature fast-neutron irradiation of pyrolytic-carbon-coated ThO2 microspheres, Carbon N. Y. 7 (1969) 373–378.
[65] J.C. Bokros, D.W. Stevens, Irradiation behavior of isotropic carbons, Carbon N. Y. 9 (1971) 19–37.
[66] P.E. Reagan, R.L. Beatty, E.L. Long, Performance of Pyrolytic carbon-coated uranium oxide particles during irradiation at high temperature, Nucl. Sci. Eng. 28 (1967) 34–41.
[67] B.J. Marsden, et al., Dimensional change, irradiation creep and thermal/mechanical property changes in nuclear graphite, Int. Mater. Rev. 61 (2016) 155–182.
[68] G.R. Bower, S.A. Ploger, P.A. Demkowicz, J.D. Hunn, Measurement of kernel swelling and buffer densification in irradiated UCO-TRISO particles, J. Nucl. Mater. 486 (2017) 339–349.
[69] T. Nozawa, Y. Katoh, J.H. Miller, Shear properties at the PyC/SiC interface of a TRISO-coating, J. Nucl. Mater. 371 (2007) 304–313.
[70] F. Cao, et al., Evaluation of thermal conductivity of the constituent layers in TRISO particles using Raman spectroscopy, J. Eur. Ceram. Soc. 37 (2017) 4457–4465.
[71] D. Frazer, J. Szornel, D.L. Krumwiede, K.A. Terrani, P. Hosemann, Evaluation of the mechanical properties of TRISO particles using nanoindentation and ring compression testing, Exp. Mech. 57 (2017) 1081–1090.
[72] B.C. Davis, L. Ward, D.P. Butt, B. Fillery, I. Reimanis, Fracture strength and principal stress fields during crush testing of the SiC layer in TRISO-coated fuel particles, J. Nucl. Mater. 477 (2016) 263–272.
[73] D. Liu, D. Cherns, Nano-cracks in a synthetic graphite composite for nuclear applications, Philos. Mag. 98 (2018) 1272–1283.